Origin of spurious oscillations in lattice Boltzmann simulations of oscillatory noncontinuum gas flows

Yong Shi, Daniel R. Ladiges, and John E. Sader

Phys. Rev. E **100**, 053317 — Published 25 November 2019

DOI: 10.1103/PhysRevE.100.053317

Origin of Spurious Oscillations in Lattice Boltzmann Simulation of Oscillatory Noncontinuum Gas Flows

Yong Shi[1*], Daniel R. Ladiges[2,3] and John. E. Sader[2†]

[1] *Department of Mechanical, Materials and Manufacturing Engineering, The University of Nottingham Ningbo China, Ningbo 315100, China*

[2] *ARC Centre of Excellence in Exciton Science, School of Mathematics and Statistics, The University of Melbourne, Victoria 3010, Australia*

[3] *Centre for Computational Sciences and Engineering, Lawrence Berkeley National Laboratory, Berkeley, California 94720, USA*

ABSTRACT

Oscillatory noncontinuum gas flows at the micro and nanoscale are characterized by two dimensionless groups: a dimensionless molecular length scale, the Knudsen number Kn , and a dimensionless frequency, θ, relating the oscillatory frequency to the molecular collision frequency. In a recent study (Phys. Rev. E **89**, 033305, 2014), the accuracy of the lattice Boltzmann (LB) method for simulating these flows at moderate-to-large Kn and θ was examined. In these cases, the LB method exhibits spurious numerical oscillations that cannot be removed through the use of discrete particle velocities drawn from higher-order Gauss-Hermite quadrature. Here, we identify the origin of these spurious effects and formulate a method to minimize their presence. This proposed method splits the linearized Boltzmann Bhatnagar-Gross-Krook (BGK) equation into two equations: (1) a homogeneous "gain-free equation" that can be solved directly, containing terms responsible for the spurious oscillations; and (2) an inhomogeneous "remainder equation" with homogeneous boundary conditions (i.e., stationary boundaries) that is solved using the conventional LB algorithm. This proposed "splitting method" is validated using published high-accuracy numerical solutions to the linearized Boltzmann BGK equation where excellent agreement is observed.

* Yong.Shi@nottingham.edu.cn.
† Author to whom correspondence should be address: jsader@unimelb.edu.au.

I. INTRODUCTION

The lattice Boltzmann (LB) method has its origins in the lattice gas cellular automata [1], where it was devised to remove statistical noise caused by Boolean operations. Over the past three decades, the LB method has been developed significantly [2,3], including introduction of the Bhatnagar-Gross-Krook (BGK) collision operator [4], multiphase capability allowing for interphase interactions [5–7], decoupled particle velocities from temporal-spatial discretization [8–10], and multi-relaxation-time collision models [11]. Introduction of the BGK collision operator led to the prevalent LB BGK method [12,13], which was later shown to be a numerical scheme for solving the Boltzmann BGK equation [14,15]. The LB method is now applied widely to simulate fluid transport of scientific and engineering relevance [16–19].

The above-mentioned link between the LB BGK model and the Boltzmann BGK equation has spurred interest in using the LB BGK method to simulate noncontinuum gas flows that naturally occur at the micro and nanoscales [20–31]. It is known that these flows depart from continuum Navier-Stokes descriptions [32], with the deviations captured by solutions to the Boltzmann BGK equation [33]. Even so, existing LB BGK models exhibit poor accuracy for these noncontinuum flows [34]. This is in contrast to their demonstrated success in simulating macroscopic (continuum) flows. One reason underlying this issue is the widespread use of standard discrete particle velocity sets that are formulated using Gauss-Hermite (GH) quadrature for continuum (near-equilibrium) flows. Noncontinuum flows at the micro and nanoscales strongly deviate from equilibrium.

A number of modifications have been introduced to the LB framework to address this issue. Early proposals include the use of kinetic boundary conditions at solid walls [20] and an effective mean free path to account for rarefied effects near walls [21,22]. These approaches make use of the standard LB algorithm and particle velocity set, while achieving improved accuracy in the low Knudsen number slip regime. Later research focused on larger Knudsen numbers by modifying the discrete particle velocities. The velocity sets for continuum flows have been increased using higher-order full-space Gauss-Hermite (FGH) quadrature [23-25], half-space Gauss-Hermite (HGH) quadrature [26-28], and other Gauss quadrature rules [29]. These allow for enhanced numerical description of the distribution function over the particle velocity space, improving the accuracy of moment evaluation.

Importantly, noncontinuum flows arise not only at finite and large Knudsen numbers, $\mathrm{Kn} = \lambda / L$, where λ is the gas mean free path and L is the hydrodynamic characteristic length scale, but also under highly unsteady conditions. Micro- and nano-electromechanical systems often feature resonating

structures that oscillate at high frequencies, inherently generating such unsteady flows [35]. In these practical settings, both spatial and temporal noncontinuum effects can arise. Temporal effects are characterized by the frequency ratio, $\theta = \omega\tau$, where ω and τ are the oscillation frequency and molecular relaxation time, respectively. A variety of numerical methods, based on the Boltzmann-BGK equation or its linearized form, have been used to study noncontiuum oscillatory flows between plates and inside cavities [36-41]. In the context of the LB method, Shi *et al*. [42] investigated the numerical performance of a hierarchy of FGH LB models using simulations of oscillatory Couette flows at different Kn and θ values. Strong spurious oscillations in the velocity field were evident at large θ, the origin of which remained unknown. Use of higher-order FGH LB models did not alleviate these spurious features which tended to overwhelm key flow characterisitics.

Here we explore this issue, identify its cause, and formulate a new method that minimizes these spurious oscillations. We find that evaluation of the moments using the discrete particle velocity set underlies these effects. At a high frequency, the distribution function is strongly oscillatory which makes these moment evaluations problematic. This issue is addressed by splitting the linearized Boltzmann BGK equation into two equations: (i) a "gain-free equation" [40], and (ii) a "remainder equation". We solve the gain-free equation directly using the method of characteristics, circumventing the use of the LB method, while the remainder equation is solved numerically using FGH and HGH LB models. This approach is found to drastically reduce the appearance of spurious oscillations. Similar yet different splitting treatments have been used previously in the kinetic theory of gases to deal with the propagation of boundary-induced discontinuities [40, 43-46].

The article is organized as follows: In Section II, we study the linearized Boltzmann BGK equation for oscillatory Couette flows. By analyzing the resulting distribution function in particle velocity space, we explain the origin of the aforementioned spurious oscillations. We then describe the proposed splitting method in Section III, where the resulting gain-free equation is solved analytically for oscillatory Couette flows. An off-lattice LB model is used to solve the remainder equation. In Section IV, we present numerical results for oscillatory Couette flows using the splitting method. These results are compared to existing high-accuracy solutions to the linearized Boltzmann BGK equation. Concluding remarks are given in Section V.

II. LINEARIZED BOLTZMANN BGK EQUATION FOR OSCILLATORY COUETTE FLOWS

We consider a flow generated in a gas confined between two parallel solid plates that oscillate in their

planes, i.e., oscillatory Couette flow. The distance between the plates is L and they move in opposite directions at identical speeds, $\hat{u}_w$; see Fig. 1.

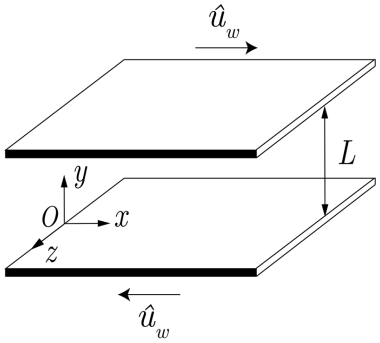

FIG. 1. Schematic of oscillatory Couette flow. The origin of the fixed (inertial) coordinate system is at the center line of the bottom plate. It is fixed in the laboratory frame.

This flow can be described in the frequency domain by the "steady-state" solution of a virtual time-dependent linearized Boltzmann BGK equation [47],

$$\frac{\partial \hat{h}}{\partial t'} + \mathbf{c} \cdot \frac{\partial \hat{h}}{\partial \mathbf{r}} = -\frac{\hat{h}}{\tau^*} + \frac{\hat{h}^{eq}}{\tau}, \tag{1}$$

where $\hat{h}$ is the frequency-based distribution function that defines the (linearized) perturbation to the true distribution function of the gas [42,47]. The variables, t', $\mathbf{r}$ and $\mathbf{c}$, represent the virtual time, particle position and particle velocity, respectively. The relaxation time, τ, originates from the BGK model [4], and a complex-valued relaxation time arises, $\tau^* \triangleq \tau/(1+\omega\tau i)$. Here, ω is the (applied) oscillatory frequency and i is the usual imaginary unit. The local equilibrium perturbation, $\hat{h}^{eq}$, is

$$\hat{h}^{eq} = \frac{\delta\hat{\rho}}{\rho_0} + \frac{\mathbf{c}\cdot\hat{\mathbf{u}}}{RT_0} + \left(\frac{\mathbf{c}^2}{2RT_0} - \frac{D}{2}\right)\frac{\delta T}{T_0}, \tag{2}$$

where D is the dimensionality of physical space and R is the gas constant. ρ_0 and T_0 represent the reference fluid density and temperature at global equilibrium, respectively. In the low Mach number (linear) limit, the density and temperature perturbations in oscillatory Couette flows are zero, i.e., $\delta\hat{\rho} = 0$ and $\delta T = 0$ [42]; the flows are isothermal. The bulk fluid velocity in Eq. (2) is

$$\hat{\mathbf{u}} = \int \frac{f_0^{eq}}{\rho_0} \hat{h}\mathbf{c}\, d\mathbf{c}, \tag{3}$$

where f_0^{eq} is the global Maxwellian of the quiescent fluid at density ρ_0 and temperature T_0. The Maxwell diffuse boundary conditions are employed at the solid walls,

$$\hat{h}=\begin{cases}\hat{h}_w^{eq,+}=-\dfrac{c_x\hat{u}_w}{RT_0}, & \text{for } c_y>0 \text{ at } y=0,\\[2ex] \hat{h}_w^{eq,-}=\dfrac{c_x\hat{u}_w}{RT_0}, & \text{for } c_y<0 \text{ at } y=L,\end{cases} \tag{4}$$

where c_x and c_y are the components of $\mathbf{c}$ in the x and y directions. The linearized Boltzmann BGK equation, Eq. (1), is integrated along the characteristic line ($\mathbf{c}=d\mathbf{r}/dt$). Applying the boundary conditions in Eq. (4), together with Eq. (2), then gives

$$\hat{h}=\begin{cases}h_w^{eq,+}\exp\left(-\dfrac{aY}{\zeta_y}\right)+\dfrac{\sqrt{\pi}}{2Kn\cdot\zeta_y}\displaystyle\int_0^Y\exp\left(\frac{a}{\zeta_y}\left(Y'-Y\right)\right)\cdot\hat{h}^{eq}\left(Y'\right)\,dY', & \text{for } \zeta_y>0\ ;\\[2ex] h_w^{eq,-}\exp\left(\dfrac{a\left(1-Y\right)}{\zeta_y}\right)-\dfrac{\sqrt{\pi}}{2Kn\cdot\zeta_y}\displaystyle\int_Y^1\exp\left(\frac{a}{\zeta_y}\left(Y'-Y\right)\right)\cdot\hat{h}^{eq}\left(Y'\right)\,dY', & \text{for } \zeta_y<0\ ,\end{cases} \tag{5}$$

where $a=\sqrt{\pi}\left(1+\theta i\right)/\left(2Kn\right)$ and $\mathrm{Kn}=\sqrt{\pi RT_0}\tau/\left(\sqrt{2}L\right)$. The dimensionless spatial coordinates are $\left(X,Y\right)=\left(x,y\right)/L$, whereas the dimensionless particle velocities are $\left(\zeta_x,\zeta_y\right)=\left(c_x,c_y\right)/\sqrt{2RT_0}$.

A. Effect of discontinuity of the distribution function in particle velocity space

Importantly, the discontinuity in $\hat{h}$ about $c_y=0$ exists at every point in the flow region, see Eq. (5); ζ_y is in the denominator of each term. This discontinuity results from the boundary condition in Eq. (4), and can be robustly handled through the use of half-space quadrature, which integrates the regions $c_y<0$ and $c_y>0$, separately. We therefore apply the half-space LB model to solve Eq. (1) and simulate oscillatory Couette flows at large θ. The use of half-space quadrature still result in spurious oscillations similar to those observed in previous LB modeling [42]; see results in Section IV A. Therefore, the discontinuity in particle velocity space cannot account for these spurious oscillations.

B. Oscillatory component of the distribution function

The first terms in Eq. (5) are complex-valued exponential functions, which we refer to as $\hat{h}_{\mathrm{osc}}$ for convenience:

$$\hat{h}_{\text{osc}} = \begin{cases} \hat{h}_w^{eq,+} \exp\left(-\dfrac{aY}{\zeta_y}\right), & \zeta_y > 0, \\ \hat{h}_w^{eq,-} \exp\left(\dfrac{a(1-Y)}{\zeta_y}\right), & \zeta_y < 0. \end{cases} \tag{6}$$

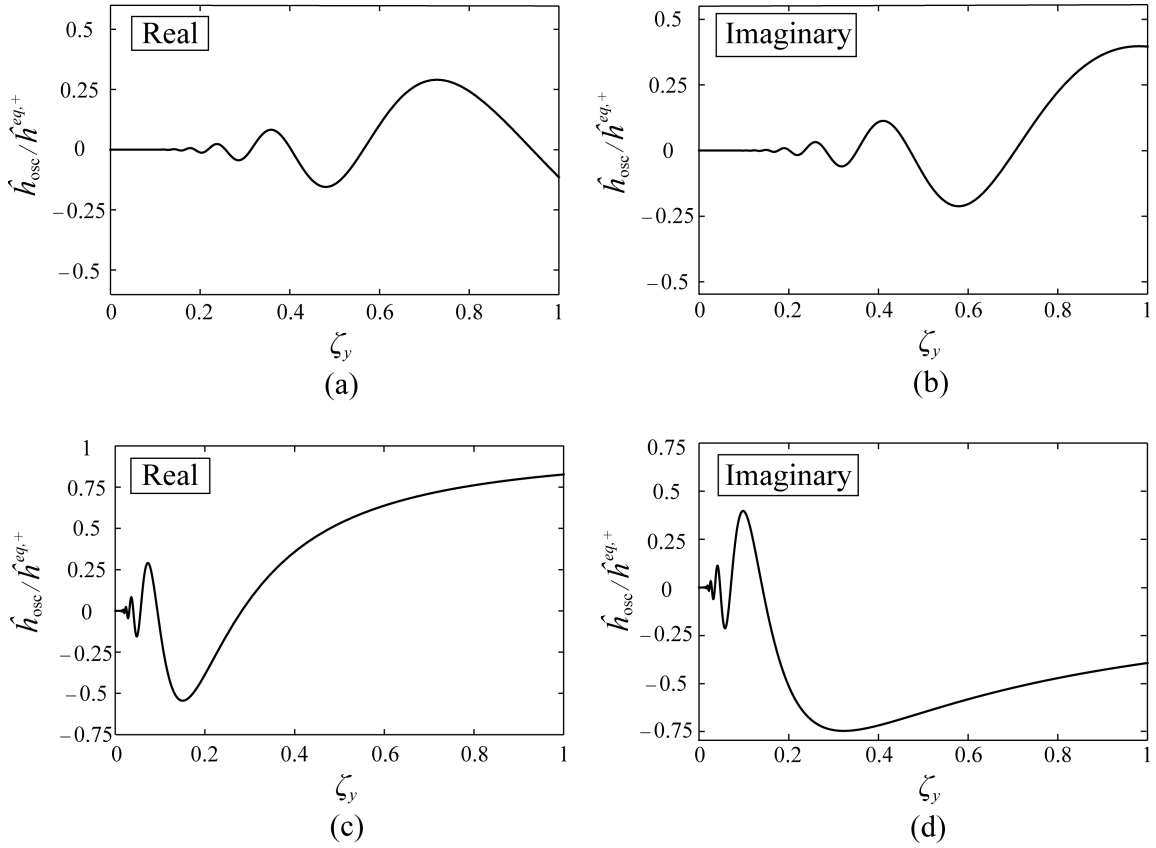

FIG. 2. The profiles of $\hat{h}_{\text{osc}}\left(\zeta_x \neq 0, \zeta_y > 0\right)\big/\hat{h}_w^{eq,+}$ at $Y = 1/10$ and $\theta = 5$. The top row: $\text{Kn} = 1/10$; The bottom row: $\text{Kn} = 1$.

Note that $\hat{h}_{\text{osc}}$ is symmetric about $\left(\zeta_x, \zeta_y, Y\right) = \left(0, 0, 1/2\right)$; $Y = 1/2$ refers to center of the channel. Importantly, for flows at large θ, this exponential function is a highly oscillatory function of ζ_y. Figure 2 gives results for $\hat{h}_{\text{osc}}\left(\zeta_x \neq 0, \zeta_y > 0\right)\big/h_w^{eq,+}$ at $Y = 1/10$, $\theta = 5$ and $\text{Kn} = 1/10$, 1, respectively. These results show that both the real and imaginary parts of $\hat{h}_{\text{osc}}$ are highly oscillatory, especially in the vicinity of $\zeta_y = 0$. Moreover, the amplitude and wavelength of $\hat{h}_{\text{osc}}$ grow with increasing ζ_y, and $\hat{h}_{\text{osc}}$ converges to $\hat{h}_w^{eq,+}$ for large ζ_y.

Equation (5) also contains integrals involving the equilibrium distribution function, $\hat{h}^{eq}$. Since $\hat{h}^{eq}$ is a linear combination of the moments of $\hat{h}$, these integral expressions are expected to be less oscillatory than $\hat{h}_{\text{osc}}$.

Therefore, it appears plausible that the oscillatory component, $\hat{h}_{\text{osc}}$, drive the spurious oscillations observed in previous LB simulations [42]. Importantly, $\hat{h}_{\text{osc}}$, in Eq. (6), is the solution to the linearized Boltzmann BGK equation, Eq. (1), but with the gain term, $\hat{h}^{eq}$, omitted. We henceforth refer to this modified equation as the "gain-free equation". This will form a key component of the proposed "splitting method", which is discussed in the next section.

III. THE SPLITTING METHOD

Equations (1) and (4) form an inhomogeneous linear system, which can always be split into two linear systems, solved independently, and then combined to obtain the required solution. We therefore split the original distribution function, $\hat{h}$, into two components, i.e., $\hat{h} = \hat{h}^{(1)} + \hat{h}^{(2)}$. The first distribution function, $\hat{h}^{(1)}$, is chosen to satisfy the "gain-free equation",

$$\frac{\partial \hat{h}^{(1)}}{\partial t'} + \mathbf{c} \cdot \frac{\partial \hat{h}^{(1)}}{\partial \mathbf{r}} = -\frac{1}{\tau^*} \hat{h}^{(1)}, \tag{7}$$

subject to the boundary conditions,

$$\hat{h}^{(1)} = \begin{cases} \hat{h}_w^{eq,\,+}, & \text{for } c_y > 0 \text{ at } y = 0, \\ \\ \hat{h}_w^{eq,\,-}, & \text{for } c_y < 0 \text{ at } y = L. \end{cases} \tag{8}$$

The "remainder equation" is the corresponding inhomogeneous equation with homogenous boundary conditions, defined by the remainder following subtraction of Eqs. (7) and (8) from Eqs. (1) and (4), i.e.,

$$\frac{\partial \hat{h}^{(2)}}{\partial t'} + \mathbf{c} \cdot \frac{\partial \hat{h}^{(2)}}{\partial \mathbf{r}} = -\frac{\hat{h}^{(2)}}{\tau^*} + \frac{\hat{h}^{(2),eq}}{\tau} + \frac{\hat{h}^{(1),eq}}{\tau}, \tag{9}$$

where

$$\hat{h}^{(1),eq} = \frac{\mathbf{c} \cdot \hat{\mathbf{u}}^{(1)}}{RT_0}, \qquad \hat{h}^{(2),eq} = \frac{\mathbf{c} \cdot \hat{\mathbf{u}}^{(2)}}{RT_0}. \tag{10}$$

$\hat{\mathbf{u}}^{(1)}$ and $\hat{\mathbf{u}}^{(2)}$ are the first-order moments of $\hat{h}^{(1)}$ and $\hat{h}^{(2)}$, respectively. The inhomogeneous linear equation, Eq. (9), is subject to homogeneous boundary conditions at the solid walls,

$$\hat{h}_w^{(2)} = \begin{cases} 0, & \text{for } c_y > 0 \text{ at } y = 0, \\ \\ 0, & \text{for } c_y < 0 \text{ at } y = L. \end{cases} \tag{11}$$

Equations (7) and (8) are solved directly (and analytically) for $\hat{h}^{(1)}$ using the method of characteristics for oscillatory Couette flows – a similar approach can be used for other flow geometries (which may require numerical computation). This is possible because Eq. (7) is not of integro-differetial form – it is a simple differential equation – unlike the original Boltzmann BGK equation, Eq. (1). Since $\hat{h}^{(1)}$ can be a highly oscillatory function of particle velocity, $\mathbf{c}$ – as observed for $\hat{h}_{\text{osc}}$ above (it satisfies the same equation, as discussed) – direct and accurate solution using the method of characteristics facilitates accurate evaluation of its corresponding moments; this will be explored below for oscillatory Couette flows.

The remainder equation, Eq. (9), for $\hat{h}^{(2)}$ is driven by a source (inhomogenous) term that contains moments of $\hat{h}^{(1)}$. These moments smooth any oscillatory behavior in $\hat{h}^{(1)}$. Thus, $\hat{h}^{(2)}$ in the remainder equation is expected to be far less oscillatory than $\hat{h}^{(1)}$. An LB method (e.g., D2Q36) is then suitable to solve this remainder equation and evaluate the corresponding moments of $\hat{h}^{(2)}$; the required moment, $\hat{\mathbf{u}}^{(1)}$ in Eq. (10), is evaluated directly and hence accurately from the solution to $\hat{h}^{(1)}$, as discussed above.

A. Gain-free solution for oscillatory Couette flows

As mentioned above, solution to Eqs. (7) and (8) is given by Eq. (6), i.e., $\hat{h}^{(1)} = \hat{h}_{\text{osc}}$, via the method of characteristics. The corresponding fluid velocity is then determined exactly by

$$\hat{\mathbf{u}}^{(1)} = \int \frac{f_0^{eq}}{\rho_0} \hat{h}^{(1)} \mathbf{c} \, d\mathbf{c} = \left(\frac{\hat{u}_w}{\sqrt{\pi}} \Psi\left(Y\right), 0 \right), \tag{12}$$

where

$$\Psi\left(Y\right) = A_0\left[a\left(1-Y\right)\right] - A_0\left(aY\right), \tag{13}$$

and $A_0\left(z\right) = \int_0^\infty \exp\left(-x^2 - z/x\right) dx$ is the zeroth-order Abramowitz function [48].

The exact solutions in Eqs. (6) and (12) are used to examine whether the conventional GH LB model can solve Eq. (7) accurately and handle the highly oscillatory distribution function, $\hat{h}^{(1)}$, and its moments. Figure 3 compares numerical solutions of the "gain-free equation" using the D2Q36 model in Ref. [42] (in terms of the LB discrete velocities $\mathbf{c}_j$) to the exact analytical solution in Eq. (6), for $\text{Kn} = 1/10$ and

$\theta = 5$. For clarity, we illustrate the exact analytical solution using black open circles with a spatial resolution, $\Delta Y = 1/100$.

Two representative distribution functions are shown for $\mathbf{c}_6(-b,b)$ and $\mathbf{c}_{28}(c,-a)$, i.e., $\hat{h}_6^{(1)}$ and $\hat{h}_{28}^{(1)}$, and the streamwise bulk velocity, $\hat{u}^{(1)}$ (the fluid velocity component in the x direction), is also given. These results are obtained using the full-space (FGH) D2Q36 model [42], denoted FD2Q36; its discrete particle velocities are defined by Eq. (16) and given in Table 1. The distribution functions $\hat{h}_6^{(1)}$ and $\hat{h}_{28}^{(1)}$ from the LB simulation (continuous red lines) are in excellent agreement with the exact analytical solution in Eq. (6) (open circles). However, the streamwise velocity, $\hat{u}^{(1)}$ (the first-order moment of $\hat{h}^{(1)}$), deviates significantly from the exact solution, Eq. (12), and presents strong (spurious) oscillations. These features are very similar to the spurious oscillations reported in Ref. [42].

Figure 3 shows that conventional FGH LB models accurately solve the "gain-free equation", Eq. (7), even for strongly noncontinuum flows at large θ, but have difficulty with the subsequent moment evaluation, e.g., for $\hat{u}^{(1)}$. This is because the discrete particle velocity set of the LB method is selected from FGH abscissae, and GH quadrature is known to perform poorly when the integrand is a highly oscillatory function of particle velocity. In Ref. [42], FGH LB models are used to evaluate the moments of $\hat{h}$, which includes the highly oscillatory function $\hat{h}^{(1)}$. This explains why these previously reported results [42] exhibit spurious numerical oscillations for flows at large θ.

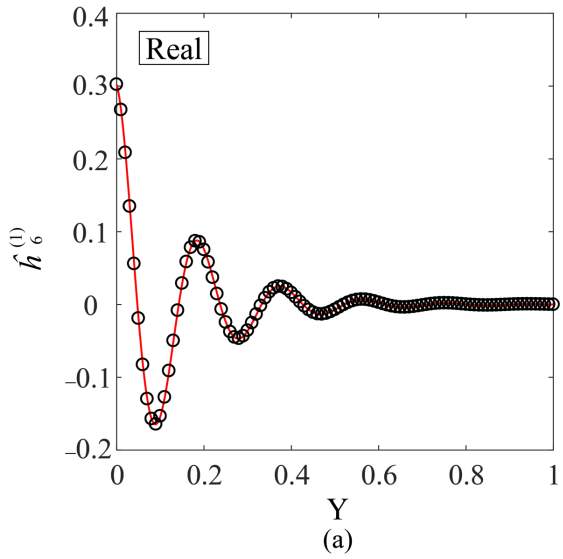
Real
$\hat{h}_6^{(1)}$
Y
(a)

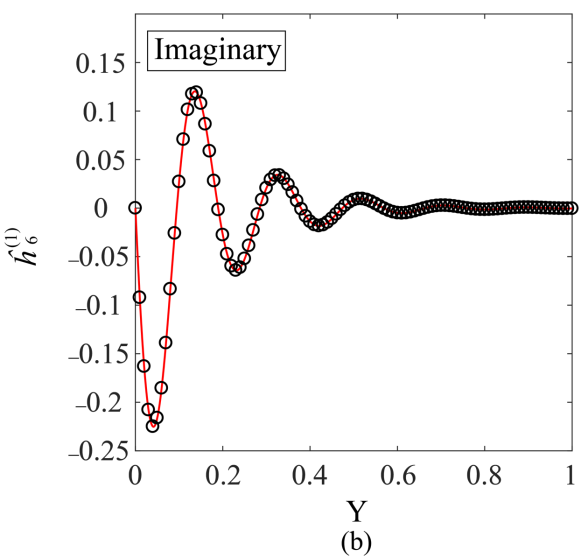
Imaginary
$\hat{h}_6^{(1)}$
Y
(b)

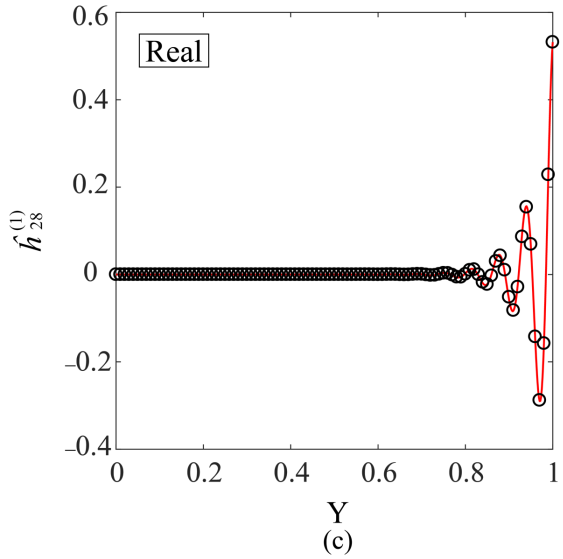
Real
$\hat{h}_{28}^{(1)}$
Y
(c)

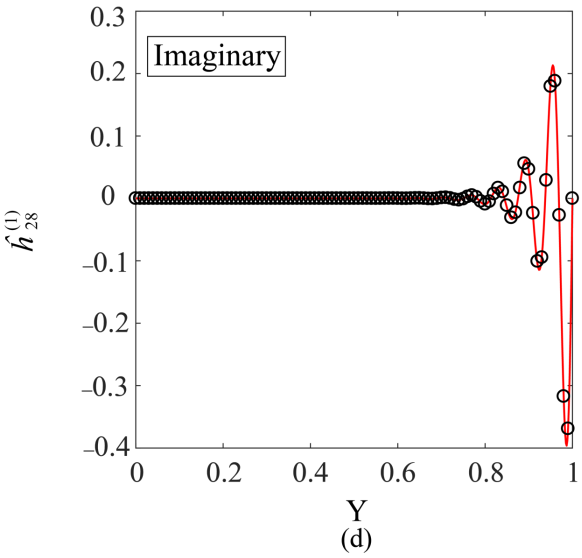
Imaginary
$\hat{h}_{28}^{(1)}$
Y
(d)

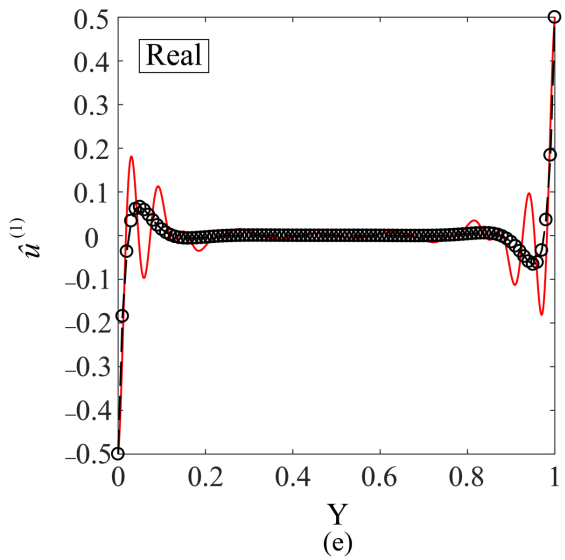
Real
$\hat{u}^{(1)}$
Y
(e)

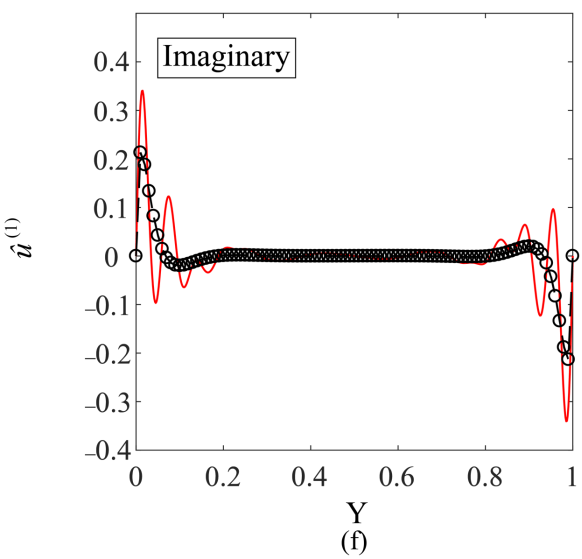
Imaginary
$\hat{u}^{(1)}$
Y
(f)

FIG 3. The profiles of $\hat{h}_6^{(1)}$, $\hat{h}_{28}^{(1)}$ and the streamwise velocity $\hat{u}^{(1)}$ for oscillatory Couette flow at $\mathrm{Kn} = 1/10$ and $\theta = 5$. FD2Q36 LB results (solid red line) [42]; analytical solution (open black circles) to Eqs. (6) and (12). Black dashed lines in (e) and (f) are included to guide the eye.

B. Lattice Boltzmann method for the remainder equation

An LB model to solve $\hat{h}^{(2)}$ is constructed using the conventional GH LB framework [42]. The discrete particle-velocity version of Eq. (9) is

$$\frac{\partial \hat{h}_j^{(2)}}{\partial t'} + \mathbf{c}_j \cdot \frac{\partial \hat{h}_j^{(2)}}{\partial \mathbf{r}} = -\frac{\hat{h}_j^{(2)}}{\tau^*} + \frac{\hat{h}_j^{(2),eq}}{\tau} + \frac{\hat{h}_j^{(1),eq}}{\tau}, \tag{14}$$

where $\hat{h}_j^{(2)}$ denotes $\hat{h}^{(2)}$ evaluated at a discrete velocity $\mathbf{c}_j$, and the corresponding equilbrium functions are

$$\hat{h}_j^{(1),eq} = \frac{\mathbf{c}_j \cdot \hat{\mathbf{u}}^{(1)}}{RT_0}, \qquad \hat{h}_j^{(2),eq} = \frac{\delta\hat{\rho}^{(2)}}{\rho_0} + \frac{\mathbf{c}_j \cdot \hat{\mathbf{u}}^{(2)}}{RT_0}. \tag{15}$$

The source term, $\hat{h}_j^{(1),eq}$ in Eq. (14), does not include its density perturbation $\delta\hat{\rho}^{(1)}$; consistent with its continuous form, $\hat{h}^{(1),eq}$, in Eq. (10). However, $\delta\hat{\rho}^{(2)}$ is included in $\hat{h}_j^{(2),eq}$, see Eq. (15), because the LB model is derived in the low-Mach number limit. This feature is used to assess its accuracy of oscillatory Couette flows by checking that $\delta\hat{\rho}^{(2)}$ vanishes.

In Eq. (14), both FD2Q36 and half-space D2Q36 (HD2Q36) schemes are used to specify $\mathbf{c}_j$,

$$\mathbf{c}_j = \begin{cases} (\pm a, \pm a), & j = 1-4, \\ (\pm b, \pm b), & j = 5-8, \\ (\pm c, \pm c), & j = 9-12, \\ (a,b)_{FS}, & j = 13-20, \\ (a,c)_{FS}, & j = 21-28, \\ (b,c)_{FS}, & j = 29-36, \end{cases} \tag{16}$$

where the subscript *FS* denotes full symmetry, and the included constants and velocity weights of the two schemes are summarized in Table 1. The corresponding moments, $\delta\hat{\rho}^{(2)}$ and $\hat{\mathbf{u}}^{(2)}$, are computed using,

$$\delta\hat{\rho}^{(2)} = \rho_0 \sum_j w_j \hat{h}_j^{(2)}, \qquad \hat{\mathbf{u}}^{(2)} = \sum_j w_j \hat{h}_j^{(2)} \mathbf{c}_j. \tag{17}$$

FD2Q36 and HD2Q36 discrete velocities do not stream among the lattice nodes in one time step. This requires the temporal and spatial discretizations to be decoupled from the discrete particle velocities. We therefore apply a finite-difference scheme [42] to discretize time and physical space in Eq. (14). This leads to an off-lattice LB evolution equation,

$$\hat{g}^{(2)}_{j,n+1} + \Delta t' \mathbf{c}_j \cdot \left(\frac{\partial \hat{h}^{(2)}_{j,n}}{\partial \mathbf{r}} \right)_{FD} = \hat{h}^{(2)}_{j,n} + \frac{1}{2}\left(\Omega \cdot \hat{h}^{(2),eq}_{j,n} - \Omega^* \cdot \hat{h}^{(2)}_{j,n} \right) + \Omega \cdot \hat{h}^{(1),eq}_{j,n}, \tag{18}$$

where n and $\Delta t'$ are the n^{th} time layer and virtual time step, respectively. The dimensionless collision frequencies are $\Omega = \Delta t'/\tau$ and $\Omega^* = \Delta t'/\tau^*$. In Eq. (18), a function $\hat{g}^{(2)}_j$ is defined to remove numerical implicitness,

$$\hat{g}^{(2)}_j = \left(1 + \frac{\Omega\theta}{2} i \right) \hat{h}^{(2)}_j + \frac{\Omega}{2}\left(\hat{h}^{(2)}_j - \hat{h}^{(2),eq}_j \right). \tag{19}$$

Using $\hat{g}^{(2)}_j$, the moments, $\delta\hat{\rho}^{(2)}$ and $\hat{\mathbf{u}}^{(2)}$, become

$$\delta\hat{\rho}^{(2)} = \frac{\rho_0}{1 + \Omega\theta i/2} \sum_j w_j \hat{g}^{(2)}_j \ , \qquad \hat{\mathbf{u}}^{(2)} = \frac{1}{1 + \Omega\theta i/2} \sum_j w_j \hat{g}^{(2)}_j \mathbf{c}_j \, . \tag{20}$$

TABLE I. Constants and velocity weights for FD2Q36 and HD2Q36 schemes.

FD2Q36 [42]	$a = 0.6167\sqrt{RT_0}$, $b = 1.8892\sqrt{RT_0}$, $c = 3.3243\sqrt{RT_0}$.	$w_{1-4} = 0.1671$, $w_{5-8} = 7.85\times10^{-3}$, $w_{9-12} = 6.53\times10^{-6}$, $w_{13-20} = 3.62\times10^{-2}$, $w_{21-28} = 1.04\times10^{-3}$, $w_{29-36} = 2.26\times10^{-4}$.
HD2Q36 [27]	$a = 0.2695\sqrt{RT_0}$, $b = 1.1996\sqrt{RT_0}$, $c = 2.5453\sqrt{RT_0}$.	$w_{1-4} = 6.33\times10^{-2}$, $w_{5-8} = 5\times10^{-2}$, $w_{9-12} = 6.09\times10^{-4}$, $w_{13-20} = 5.63\times10^{-2}$, $w_{21-28} = 6.21\times10^{-3}$, $w_{29-36} = 5.52\times10^{-3}$.

In addition, $\left(\partial\hat{h}^{(2)}_{j,n} / \partial\mathbf{r} \right)_{FD}$ on the left side of Eq. (18) represents the finite-difference approximation of the spatial derivative. As in Ref. [42], we apply a second-order upwind scheme to discretize spatial derivatives on the bulk nodes while a hybrid scheme, consisting of first-order upwind and central

difference schemes, is used for nodes next to the solid walls. Take the x component of $\left(\partial \hat{h}_{j,n}^{(2)} / \partial \mathbf{r}\right)$ as an example. The second-order upwind approximations are

$$\left.\frac{\partial \hat{h}_{j,n}^{(2)}}{\partial x}\right|_{x,y} \approx \frac{3\hat{h}_{j,n}^{(2)}(x,y) - 4\hat{h}_{j,n}^{(2)}(x-\Delta x,y) + \hat{h}_{j,n}^{(2)}(x-2\Delta x,y)}{2\Delta x}, \qquad c_{jx} > 0, \qquad (21)$$

$$\left.\frac{\partial \hat{h}_{j,n}^{(2)}}{\partial x}\right|_{x,y} \approx -\frac{3\hat{h}_{j,n}^{(2)}(x,y) - 4\hat{h}_{j,n}^{(2)}(x+\Delta x,y) + \hat{h}_{j,n}^{(2)}(x+2\Delta x,y)}{2\Delta x}, \qquad c_{jx} < 0, \qquad (22)$$

and those based on the hybrid scheme are

$$\left.\frac{\partial \hat{h}_{j,n}^{(2)}}{\partial x}\right|_{x,y} \approx \frac{(1-\varepsilon)\hat{h}_{j,n}^{(2)}(x+\Delta x,y) + 2\varepsilon\hat{h}_{j,n}^{(2)}(x,y) - (1+\varepsilon)\hat{h}_{j,n}^{(2)}(x-\Delta x,y)}{2\Delta x}, \qquad c_{jx} > 0, \qquad (23)$$

$$\left.\frac{\partial \hat{h}_{j,n}^{(2)}}{\partial x}\right|_{x,y} \approx \frac{(1+\varepsilon)\hat{h}_{j,n}^{(2)}(x+\Delta x,y) - 2\varepsilon\hat{h}_{j,n}^{(2)}(x,y) - (1-\varepsilon)\hat{h}_{j,n}^{(2)}(x-\Delta x,y)}{2\Delta x}, \qquad c_{jx} < 0. \qquad (24)$$

Δx is the lattice spacing in the x direction and ε is a numerical factor to tune the weight of first-order upwind and central difference methods in the hybrid scheme. In this article, we specify $\varepsilon = 0.05$ to ensure the LB simulation is stable while nearly second-order accurate [42]. In summary, an off-lattice LB model is made up of Eqs. (15), (16) and (18) – (24). Its discrete particle velocities are specified by Table 1.

V. RESULTS AND DISCUSSION

In this section, we examine the two possible reasons discussed in Section II for the spurious oscillations in previous LB simulations [42]: (1) The discontinuity of $\hat{h}$ about $c_y = 0$ in the flow region, and (2) the highly oscillatory variations in $\hat{h}$ in particle velocity space. We first use the HGH LB model (without the proposed splitting method) to simulate oscillatory Couette flows at large θ, and then apply the "splitting method" to examine its efficacy in simulating these flows. High-accuracy numerical results of the Boltzmann BGK equation are used as benchmarks, whose spatial resolution is $\Delta Y = 1/40$ [36].

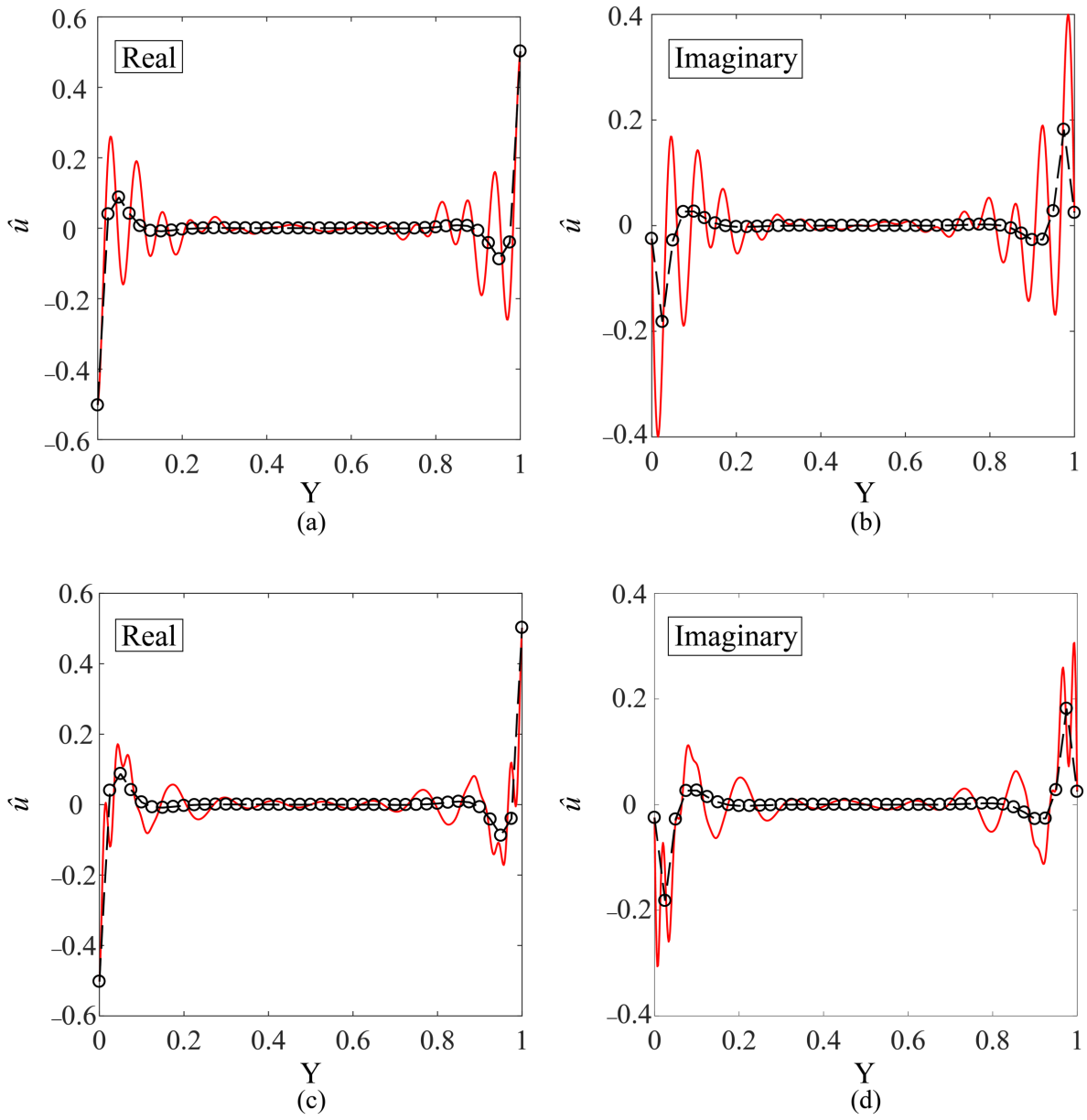

FIG. 4. The streamwise velocities, $\hat{u}$, of oscillatory Couette flow at $\mathrm{Kn} = 1/10$ and $\theta = 5$. Solid line (red): the LB results (Top row: FD2Q36; Bottom row: HD2Q36); Circles (open and black): high-accuracy Boltzmann BGK solution [36]. Black dashed lines are included to guide the eye.

A. Half-space LB simulation for oscillatory Couette flows

Unlike the results of Ref. [42] that implemented FGH LB models, HGH LB models inherently account for the distribution function discontinuity in particle velocity space. We therefore initially assess whether HGH LB models are stable and free of the spurious oscillations observed in the FGH LB models [42]. The simulations of Ref. [42], which directly solved the complete linearized Boltzmann equation, Eq. (1), are repeated using the HD2Q36 model. The splitting method is not used in this initial comparison.

Figure 4 shows the streamwise velocity, $\hat{u}$, in one representative oscillatory Couette flow at $\mathrm{Kn}=1/10$ and $\theta=5$. Complex conjugates of the LB results obtained using both FD2Q36 (the same as the results in Ref. [42]) and HD2Q36 models are given, facilitating direct comparison to high-accuracy solutions of the linearized Boltzmann BGK equation [36]. Similar to FD2Q36, spurious oscillations are observed in results obtained using HD2Q36. Therefore, HGH quadrature does not suppress the large-θ LB instablity reported in Ref. [42], and we conclude that the discontinuty of $\hat{h}$ in the flow region does not drive the observed suprious oscillations.

Nonetheless, we note that numerical accuracy is slightly improved through use of HGH quadrature. Oscillatory amplitudes and freqencies in the spurious oscillations decrease relative to FGH LB simulations; compare results in the top and bottom rows of Fig. 4. This is because HGH quadrature distributes more discrete particle velocities near the discontinuity in the distribution function about $\zeta_y=0$, where the solution is most oscillatory.

B. Splitting method for oscillatory Couette flows

Next, we apply the splitting method – using both FD2Q36 and HD2Q36 LB models – to calculate $\hat{h}_j^{(2)}$ and its moments. Results are presented for $\theta=5$, and two different Knudsen numbers, $\mathrm{Kn}=1/10$ and $\mathrm{Kn}=1$. The 2D computational domain is a square between the two solid walls with a gap $L=1$. Periodic boundary conditions are employed at the two ends of this domain while the distribution functions at the solid walls are specified using Eq. (11). We choose the Mach number, $\mathrm{M}=0.16$, and reference density, $\rho_0=1$. All simulations are performed using 4×600 grids; The corresponding lattice spacings in the x and y directions are $\Delta x=L/4$ and $\Delta y=L/600$, respectively. Refined grids in the x and y directions produce an insignificant enhancement in numerical accuracy. We use a Courant-Friedricks-Lewey number, $\mathrm{CFL}=c_m\Delta t'/\Delta y$, where c_m is the maximum particle speed. It is chosen to be 0.2 to guarantee numerical stability. Results using both FGH and HGH show that $\delta\rho^{(2)}=0$ throughout the computational domain, as required.

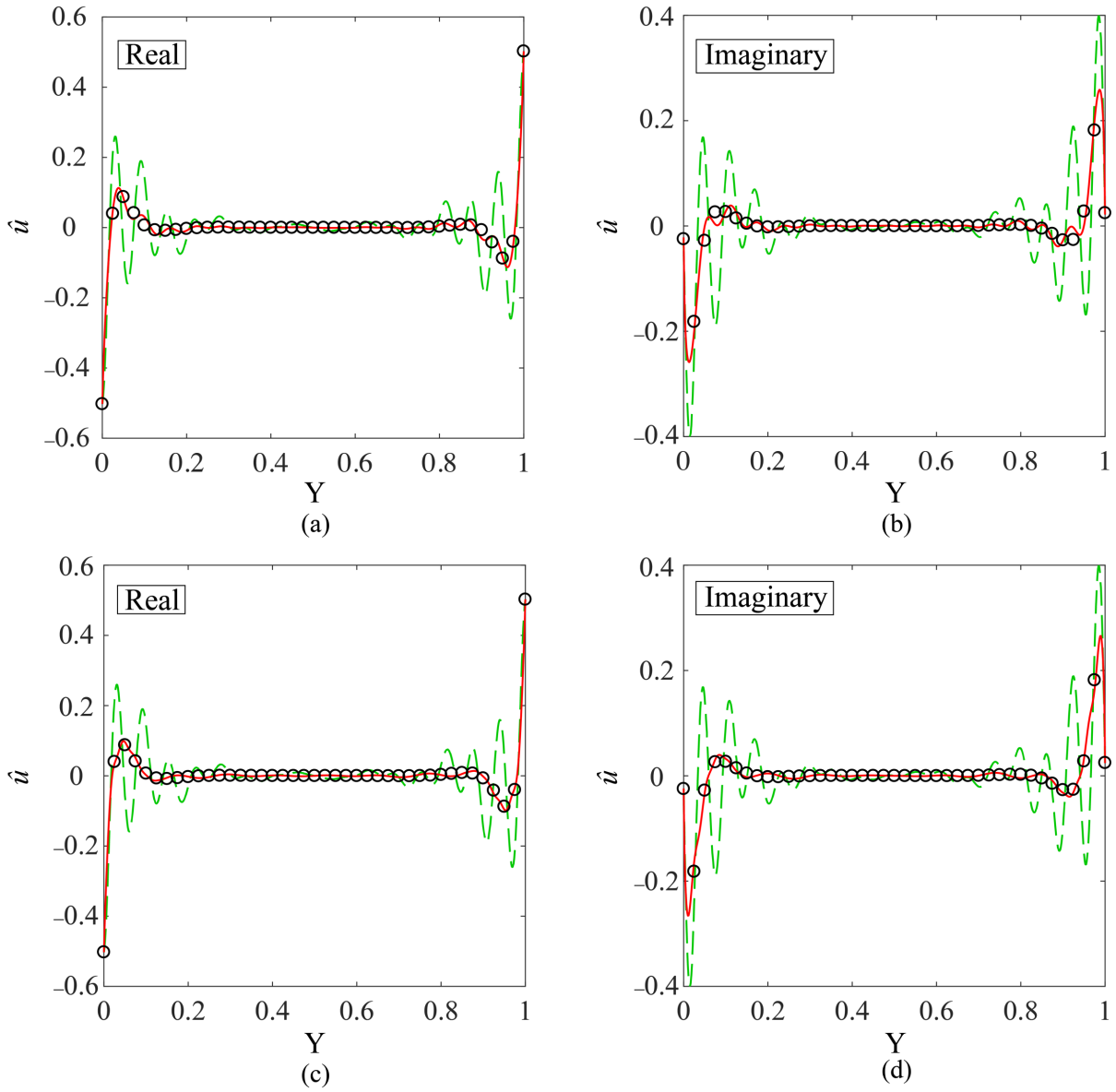

FIG. 5. The streamwise velocities, $\hat{u}$, of oscillatory Couette flow at $\mathrm{Kn}=1/10$ and $\theta=5$. Solid line (red): the present results（Top row: FD2Q36; Bottom row: HD2Q36); Circles (open and black): high-accuracy Boltzmann BGK solution [36]; Dashed line (gree): the results in Ref. [42].

The streamwise velocity, $\hat{u}$, is given in Fig. 5 for $\mathrm{Kn}=1/10$ and $\theta=5$. These results are compared to high-accuracy numerical solutions of the linearized Boltzmann BGK equation [36] and the results of Ref. [42]. Use of the splitting method with FD2Q36 produces results that agree well with the high-accuracy solutions of Ref. [36]; see Figs. 5(a) and 5(b). Strikingly, both the real and imaginary components of the streamwise velocity no longer exhibit the strong spurious oscillations of the conventional LB simulations reported in Ref. [42]. This confirms the mechanism anticipated in Section II that drives these spurious oscillations: GH quadrature is incapable of accurately computing moments

of the distribution function when it is highly oscillatory. The proposed splitting method overcomes this impediment allowing for accurate evaluation of moments and hence the streamwise velocity. Results obtained using the HD2Q36 LB model are produced in Figs. 5(c) and 5(d). This HGH LB model achieves slightly better accuracy in both the real and imaginary components, relative to the corresponding FGH LB model. Namely, the HGH velocity profiles exhibit suppressed fluctuations near the solid walls.

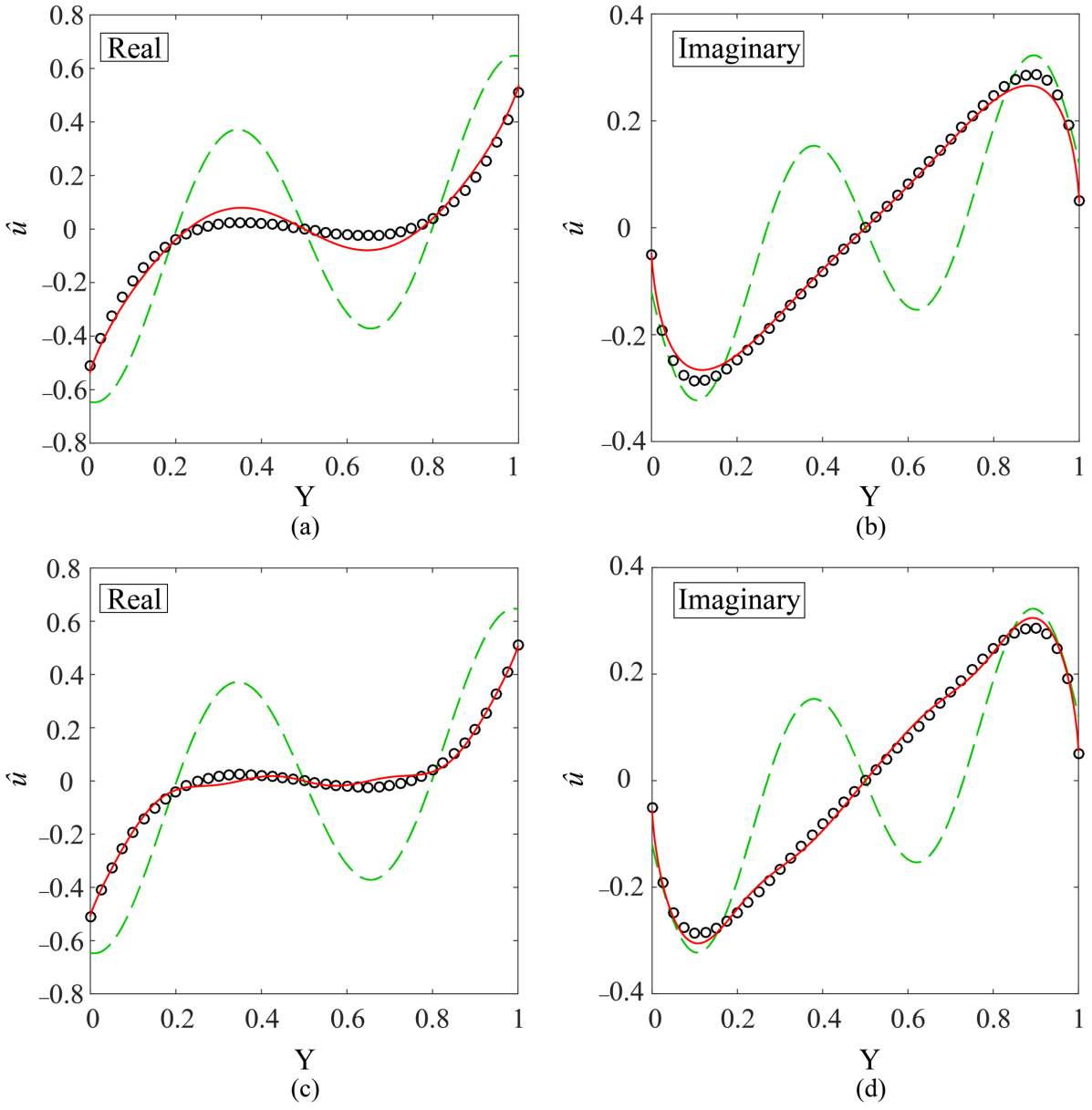

FIG. 6. The streamwise velocities, $\hat{u}$, of oscillatory Couette flow at $\mathrm{Kn}=1$ and $\theta=5$. Details as in Fig. 5.

Figure 6 shows corresponding results for $\mathrm{Kn} = 1$ and $\theta = 5$. This strongly non-equilibrium flow generates enhanced spurious oscillations relative to $\mathrm{Kn} = 1/10$ and $\theta = 5$ (see Fig. 5), when the conventional LB method is used [42]. Again, the proposed splitting method dramatically improves the situation and its results are in excellent agreement with high-accuracy numerical solutions of the Boltzmann BGK equation [36]; similar performance is achieved for higher Kn, e.g., $\mathrm{Kn} = 5$ and $\theta = 5$ (results not shown). As in the results of Fig. 5, use of HGH quadrature slightly improves accuracy, and we expect this improvement can be further enhanced through use of higher-order HGH quadrature. However, the primary suppression of spurious oscillations is achieved by the splitting method – use of HGH quadrature produces a relatively minor improvement.

V. CONCLUSIONS

We have investigated the origin of spurious oscillations in previous LB simulations of noncontinuum oscillatory Couette flows [42]. These spurious effects arise at high frequency, which this study shows are due to inaccuracy in moment evaluations of the oscillatory distribution function. Increasing the number of discrete particle velocities in the standard GH LB framework has little effect on the moment evaluation.

Spurious oscillations are suppressed through development and use of the proposed "splitting method", where the original linearized Boltzmann BGK equation is decomposed into two linear equations. The first is a homogenous "gain-free equation" subject to inhomogeneous boundary conditions – it contains the dominant oscillatory component of the complete distribution function. The "gain-free equation" is solved directly using the method of characteristics, facilitating accurate evaluation. The "remainder equation" is inhomogeneous in form with a set of homogenous boundary conditions. This inhomogeneity involves moments of the distribution function that suppresses oscillatory behavior. The remainder equation is solved using the LB method, either using full-space or half-space GH quadrature. Combination of these solutions, i.e., use of the splitting method, was shown to suppress the previously observed spurious oscillations in Ref. [42] and gave excellent agreement with published high-accuracy numerical solution of the Boltzmann BGK equation.

This splitting method circumvents the need to reformulate the current LB framework using large discrete velocity sets and/or more complex finite-difference (finite-volume) temporal-spatial schemes.

ACKNOWLEDGEMENTS

Y.S. acknowledges support from Zhejiang Provincial Natural Science Foundation of China (Grant No. LY16E060001), Ningbo Science and Technology Bureau Technology Innovation Team (Grant No. 2016B10010). D.R.L. and J.E.S. acknowledge support from the Australian Research Council Grants scheme, and the Australian Research Council Centre of Excellence in Exciton Science (CE170100026). D.R.L. also acknowledges support from the U.S. Department of Energy, Office of Science, Office of Advanced Scientific Computing Research, Applied Mathematics Program under Contract No. DE-AC02-05CH11231.

---

[1] D. A. Wolf-Gladrow, *Lattice-gas cellular automata and lattice Boltzmann models: An introduction*, (Springer-Verlag, Berlin, 2000).

[2] S. Chen, G.D. Doolen, Annu. Rev. Fluid Mech. **30**, 329 (1998).

[3] Z. L. Guo and C. Shu, Lattice Boltzmann Method and Its Applications in Engineering, (World Scientific Publishing, Singapore, 2013).

[4] P. L. Bhatnagar, E. P. Gross and M. Krook, Phys. Rev. **94**, 511 (1954).

[5] X. Shan and H. Chen, Phys. Rev. E **47**, 1815 (1993).

[6] X. He and G. Doolen, J. Stat. Phys. **107**, 309 (2002).

[7] Q. Li, K.H. Luo, Q. J. Kang, Y. L. He, Q. Chen and Q. Liu, Prog. Energy Combust Sci. **52**, 62 (2016)

[8] N. Cao, S. Chen and S. Jin and D. Martinez, Phys. Rev. E **55**, R21(R) (1997)..

[9] R. Mei and W. Shyy, J. Comput. Phys. **143**, 426 (1998).

[10] Z. L. Guo and T. S. Zhao, Phys. Rev. E 67, 066709 (2002).

[11] P. Lallemand, L. S. Luo, Phys. Rev. E **61**, 6546 (2000).

[12] H. Chen, S. Chen and W. H. Matthaeus, Phys. Rev. A. **45**, R5339 (1992).

[13] Y. H. Qian, D. D'Humieres and P. Lallemand, Europhys. Lett. **17**, 479 (1992).

[14] X. He and L. S. Luo, Phys. Rev. E **56**, 6811 (1997).

[15] X. Shan and X. He, Phys. Rev. Lett. **80**, 65 (1998).

[16] D. Yu, R. Mei, L. S. Luo and W. Shyy, Prog. Aerosp. Sci. **39**, 329 (2003).

[17] Y.L. He, Q. Li, Y. Wang and G. Tang, Chinese Sci. Bull. **54**, 4117 (2009).

[18] C. K. Aidun and J. R. Clausen, Annu. Rev. Fluid Mech. **42**, 439 (2010).

[19] A. Xu, W. Shyy and T. S. Zhao, Acta Mech. Sinica **33**, 555 (2017).

[20] S. Ansumali and I. V. Karlin, Phys. Rev. E **66**, 026311 (2002).

[21] Y. H. Zhang, X. J. Gu, R. W. Barber and D. R. Emerson, Phys. Rev. E **74**, 046704 (2006).

[22] Z. L. Guo, B. C. Shi and C. G. Zheng, Europhys. Lett. **80**, 24001 (2007).

[23] X. Shan, X. F. Yuan and H. Chen, J. Fluid Mech. **550**, 413 (2006).

[24] S. H. Kim, H. Pitsch and I. D. Boyd, J. Comput. Phys. **227**, 8655 (2008).

[25] Y. Shi, P.L. Brookes, Y. W. Yap and J. E. Sader, Phys. Rev. E **83**, 045701(R) (2011).

[26] G. P. Ghiroldi and L. Gibelli, Commun. Comput. Phys. **17**, 1007 (2015).

[27] Y. Shi, Y. W. Yap and J. E. Sader, Phys. Rev. E **92**, 013307 (2015).

[28] V. E. Ambrus and V. Sofonea, J. Comput. Phys. **316**, 760 (2016).

[29] V. E. Ambrus and V. Sofonea, Phys. Rev. E **89**, 041301 (2014).

[30] Z. L. Guo, K. Xu and R. Wang, Phys. Rev. E **88**, 033305 (2013).

[31] Z. L. Guo, R. Wang and K. Xu, Phys. Rev. E **91**, 033313 (2015).

[32] G. E. Kamiadakis, A. Beskok and N. Aluru, *Microflows and nanoflows: Fundamental and simulations* (Springer-Verlag, New York, 2005).

[33] C. Cercignani, *Rarefied gas dynamics: From basic concepts to actual calculations* (Cambridge University Press, Cambridge, 2000).

[34] C. Shen, D. B. Tian, C. Xie and J. Fan, Microsc. Therm. Eng. **8**, 423 (2004).

[35] K. Jensen, K. Kim and A. Zettle, Nat. Nanotechnol. **3**, 533 (2008).

[36] Y. W. Yap and J. E. Sader, Phys. Fluids **24**, 032004 (2012).

[37] A. Frangi, A. Frezzotti and S. Lorenzani, Comput. Struct. **85**, 810 (2007).

[38] L. Wu, J.M. Reese and Y. H. Zhang, J. Fluid Mech. **748**, 350 (2014).

[39] P. Wang, W. Su and Y. H. Zhang, Phys. Fluids **30**, 102002 (2018).

[40] D. R. Ladiges and J. E. Sader, Phys. Rev. Fluids **3**, 053401 (2018).

[41] A. Tsimpoukis, N. Vasileiadis, G. Tatsios and D. Valougeorgis, Phys. Fluids **31**, 067108 (2019).

[42] Y. Shi, Y. W. Yap and J. E. Sader, Phys. Rev. E **89**, 033305 (2014).

[43] K. Aoki, C. Bardos, C. Dogbe and F. Golse, Math. Models Methods Appl. **9**, 1581 (2001).

[44] S. Naris and D. Valougeorgis, Phys. Fluids **17**, 097106 (2005).

[45] S. Naris and D. Valougeorgis, Phys. Fluids **19**, 067103 (2007).

[46] F. Sharipov and D. Kalempa, Microfluid Nanofluid **4**, 363 (2008).

[47] Y. Shi and J.E. Sader, Phys. Rev. E **81**, 036706 (2010).

[48] *Handbook of mathematical functions with formulas, graphs and mathematical tables*, edited by M. Abramowitz and I.A. Stegun (Dover, New York, 1972).